

Role of high-order lattice anharmonicity in the phonon thermal transport of silver halide AgX ($X = \text{Cl}, \text{Br}, \text{I}$)

Niuchang Ouyang¹, Zezhu Zeng^{1,2,*}, Chen Wang¹, Qi Wang³, and Yue Chen^{1,†}

¹*Department of Mechanical Engineering, The University of Hong Kong, Pokfulam Road, Hong Kong SAR, China*

²*Institute of Science and Technology Austria, Am Campus 1, 3400 Klosterneuburg, Austria*

³*Thermal Science Research Center, Shandong Institute of Advanced Technology, Jinan, Shandong Province 250103, China*



(Received 4 May 2023; revised 16 August 2023; accepted 3 October 2023; published 8 November 2023)

The phonon transport mechanisms and ultralow lattice thermal conductivities (κ_L) in silver halide AgX ($X = \text{Cl}, \text{Br}, \text{I}$) compounds are not yet well understood. Herein, we study the lattice dynamics and thermal property of AgX under the framework of perturbation theory and the two-channel Wigner thermal transport model based on accurate machine learning potentials. We find that an accurate extraction of the third-order atomic force constants from largely displaced configurations is significant for the calculation of the κ_L of AgX, and the coherence thermal transport is also non-negligible. In AgI, however, the calculated κ_L still considerably overestimates the experimental values even including four-phonon scatterings. Molecular dynamics (MD) simulations using machine learning potential suggest an important role of the higher-than-fourth-order lattice anharmonicity in the low-frequency phonon linewidths of AgI at room temperature, which can be related to the simultaneous restrictions of the three- and four-phonon phase spaces. The κ_L of AgI calculated using MD phonon lifetimes including full-order lattice anharmonicity shows a better agreement with experiments.

DOI: [10.1103/PhysRevB.108.174302](https://doi.org/10.1103/PhysRevB.108.174302)

I. INTRODUCTION

Recently, silver halide AgX ($X = \text{Cl}, \text{Br}, \text{I}$) compounds that exhibit promising photoelectrochemical and photocatalytic properties became attractive for applications in photovoltaic devices [1,2]. Efficient thermal transport is crucial in such devices to prevent heat accumulation and to ensure optimal performance. The thermal transport properties of AgX are also relevant to their potential use as solid-state electrolytes [3], which are crucial components in advanced energy storage and conversion systems, such as solid-state batteries and fuel cells. Understanding the heat transfer characteristics of AgX can help optimize their use as electrolytes and minimize energy losses due to thermal inefficiency. However, a better understanding of the phonon thermal transport mechanisms of AgX is still in its infancy. A further study of the thermal transport properties of silver halide AgX is necessary for the development and optimization of various technological applications, including photovoltaic devices, solid-state electrolytes, and thermal management systems.

Yang *et al.* [4] reported ultralow κ_L of 0.20 and 0.18 $\text{W m}^{-1}\text{K}^{-1}$ for AgCl and AgBr at 300 K based on the conventional phonon gas model and first-principles calculations. Xia *et al.* [5] also calculated the κ_L of AgCl (0.6 $\text{W m}^{-1}\text{K}^{-1}$ at 300 K) by further including four-phonon scatterings and coherence contribution in the unified theory (UT) of thermal transport [6]. However, these theoretical studies still underestimate the experimental values of 1.10 (AgCl) and 1.05 $\text{W m}^{-1}\text{K}^{-1}$ (AgBr) [7]. In addition, Goetz *et al.* [8]

reported an ultralow experimental κ_L of 0.42 $\text{W m}^{-1}\text{K}^{-1}$ at 300 K for AgI. Although Yan *et al.* [9] revealed that the fourth-order lattice anharmonicity is significant for the calculation of κ_L of AgI, the roles of higher-than-fourth-order phonon scatterings and the coherence thermal transport are not yet ascertained.

Atomic-level understanding of phonon-phonon scatterings plays a vital role in lattice thermal transport. Generally, three-phonon scattering is adequate to describe the lattice dynamics of the majority of crystals, while the four-phonon process has recently been demonstrated to play a significant role in strongly anharmonic materials with ultralow κ_L [10–12] and materials such as BAs [13] and TaN [14] that have severely restricted three-phonon phase space (P_3). Moreover, the considerable role of higher-than-fourth-order phonon scatterings was reported in Ti_3VSe_4 [15] and zinc-blende III-V compounds [16] such as InP, BN, and InAs. Phonon frequency renormalization was also demonstrated in recent studies to be significant to predict the thermal property of strongly anharmonic materials, such as perovskites SrTiO_3 [17] and $\text{Cs}_2\text{PbI}_2\text{Cl}_2$ [18], and clathrate $\text{Ba}_8\text{Ga}_{16}\text{Ge}_{30}$ [19].

In this work, using accurate machine learning neuroevolution potentials (NEP) [20], we systematically investigate the lattice dynamics and thermal transport of AgX based on perturbation theory (PT) and the two-channel UT including both the population and coherence contributions [6,21]. We show that the accurate extraction of the third-order interatomic force constants (IFCs) and the coherence contribution are of great importance to calculate the κ_L of AgX. For AgI, however, we find that the calculated κ_L significantly overestimates the experimental values [8] even after considering the renormalizations of the third- and fourth-order IFCs and the UT. The phonon linewidths calculated using the normal-mode-

*zzeng@ist.ac.at

†yuechen@hku.hk

decomposition technique [22] based on molecular dynamics (MD) simulations [23] and NEP [20] indicate an important role of the higher-than-fourth-order phonon scatterings in AgI, which can be ascribed to the restrictions of the three- (P_3) and four-phonon phase spaces (P_4). Consequently, κ_L computed using MD phonon lifetimes within the UT shows a better agreement with the experimental results of AgI.

II. METHODS

Density functional theory (DFT) calculations of AgX are performed using the Vienna *ab initio* Simulation Package (VASP) [24] with the projector augmented wave (PAW) [25] method. The PBEsol [26] exchange-correlation functional is applied for all VASP calculations because the lattice parameters that it predicts well compare with the experiments, as shown in Table S1 of Supplemental Material (SM) [27]. We did not consider the effect of the thermal expansion since the lattice parameters of AgX undergo a minor change (<0.5%) over a temperature range of 300 K [28]. A plane-wave energy cutoff of 500 eV and an energy convergence criterion of 10^{-8} eV are used in the self-consistent electronic calculations. Born effective charges and dielectric constants are included in our calculations. We construct the machine learning NEP [20] based on the accurate DFT calculations of structures generated from *ab initio* MD simulations with a 250-atom supercell at temperatures up to 400 K under *NVT* ensemble. The renormalized second-order IFCs (IFCs2_TDEP) are extracted using the temperature-dependent effective potential (TDEP) scheme as implemented in the HIPHIVE package [29], following the work of Hellman *et al.* [30,31]. GPUMD simulations [32] based on the NEP are performed at different temperatures, and 40 configurations at each temperature are extracted to fit the temperature-dependent cubic (IFCs3_MD) and quartic IFCs (IFCs4_MD). IFCs2_FDM and IFCs2_RDM are extracted using the finite displacement method (FDM) and rattle-displacement method (RDM), respectively. We also fit the third-order IFCs (IFCs3_RDM) via the RDM from a normal distribution with a standard deviation of 0.025 Å. Note that we subtract the harmonic contributions (0 K) from the total forces prior to fitting anharmonic IFCs [33]. The neighboring cutoff distances for pairs, triplets, and quadruplets of AgX are 8.0, 7.0, and 6.0 Å, respectively. A q mesh of $12 \times 12 \times 12$ and a *scalebroad* value of 0.5 are found to be adequate to obtain accurate phonon lifetimes of AgX. We use q meshes of $18 \times 18 \times 18$ and $16 \times 16 \times 16$ for the calculation of the weighted phase space (WPS) for AgCl and AgI, respectively. The WPS is defined as the sum of frequency-containing factors in the expression of three phonon transition probabilities and is expressed [34] as

$$W_\lambda^\pm = \frac{1}{2N} \sum_{\lambda', \lambda''} \left[\frac{2(f_{\lambda'}^0 - f_{\lambda''}^0)}{f_{\lambda'}^0 + f_{\lambda''}^0 + 1} \right] \frac{\delta(\omega_\lambda \pm \omega_{\lambda'} - \omega_{\lambda''})}{\omega_\lambda \omega_{\lambda'} \omega_{\lambda''}}, \quad (1)$$

where N is the number of uniformly spaced q points in the Brillouin zone, and W_λ^\pm represents the absorption (+) and emission (−) processes.

Phonon power spectra are obtained by projecting the atomic velocities from MD simulations with NEP onto the temperature-dependent phonon eigenvectors using the

normal-mode-decomposition technique [22]. Lattice thermal conductivity ($\kappa_L^{\text{p+c}}$) is contributed by diagonal (population κ_L^{p}) and off-diagonal (coherence κ_L^{c}) terms following the UT proposed by Simoncelli *et al.* [6]. The κ_L^{c} , which originates from the wave-like tunneling of phonons, can be expressed as

$$\begin{aligned} \kappa_L^{\text{c}} = & \frac{\hbar^2}{k_B T^2 N V} \sum_{\mathbf{q}} \sum_{j, j'}^{j \neq j'} \frac{\omega(\mathbf{q})_j + \omega(\mathbf{q})_{j'}}{2} U(\mathbf{q})_{j, j'} U(\mathbf{q})_{j', j} \\ & \times \frac{\omega(\mathbf{q})_j n(\mathbf{q})_j [n(\mathbf{q})_j + 1] + \omega(\mathbf{q})_{j'} n(\mathbf{q})_{j'} [n(\mathbf{q})_{j'} + 1]}{4[\omega(\mathbf{q})_j - \omega(\mathbf{q})_{j'}]^2 + [\gamma(\mathbf{q})_j + \gamma(\mathbf{q})_{j'}]^2} \\ & \times [\gamma(\mathbf{q})_j + \gamma(\mathbf{q})_{j'}], \end{aligned} \quad (2)$$

where V is the volume of the unit cell, T is the temperature, N is the total number of sampled wave vectors and k_B is the Boltzmann constant. $n(\mathbf{q})_j$, $\omega(\mathbf{q})_j$, and $\gamma(\mathbf{q})_j$ are the equilibrium Bose-Einstein distribution, phonon frequency, and phonon linewidth for branch j at wave vector \mathbf{q} , respectively. $U(\mathbf{q})_{j, j'}$ are the off-diagonal terms of the velocity matrix when $j \neq j'$. We note that κ_L^{p} can be calculated from Eq. (1) based on the phonon gas model when $j = j'$. Additionally, the temperature-dependent κ_L of AgI is also calculated from homogeneous nonequilibrium molecular dynamics (HNEMD) simulations [35,36].

III. RESULTS AND DISCUSSION

To understand the discrepancy between experiments [37–39] and the existing first-principles calculation [4] for the κ_L of AgCl, we first compute the κ_L^{p} using the IFCs2_FDM and IFCs3_RDM with the PBE functional. It is seen from Fig. 1(a) that our result is close to that of Yang *et al.* [4]. Note that the third-order IFCs of Yang *et al.* were extracted using the PHONO3PY package [40] with an atomic displacement of 0.03 Å. Similarly to the results of Yang *et al.* [4], our κ_L^{p} also significantly underestimates the experiments [37–39]. Despite the coherence term being included, the $\kappa_L^{\text{p+c}}$ is still lower than the experimental values. After applying PBEsol functional rather than PBE, the κ_L^{p} largely increases from 0.187 to 0.425 $\text{W m}^{-1} \text{K}^{-1}$ at 300 K, as displayed in Figs. S4(a) and S4(b) of the SM [27]. Despite a considerable improvement being achieved for the calculated κ_L^{p} of AgCl when the PBEsol functional is used instead of the PBE functional, the $\kappa_L^{\text{p+c}}$ still significantly underestimates the experimental values.

We then study the phonon frequency renormalization of AgCl using the TDEP method [30,31] based on NEP from 150 to 300 K, as displayed in Fig. S3(a), where experimental values [41] of AgCl at 78 K are also included, showing a good agreement with our calculations. The phonon frequencies of AgCl generally show a weak temperature dependence, suggesting that the phonon frequency renormalization plays a minor role in predicting the κ_L of AgCl. This is different from AgI, as shown in Fig. S3(b), or other strongly anharmonic materials such as perovskites SrTiO₃ [17] and Cs₂PbI₂Cl₂ [18], and clathrate Ba₈Ga₁₆Ge₃₀ [19], where the frequencies of low-frequency phonons show significant temperature dependence. Therefore, when we replace IFCs2_FDM with the temperature-renormalized IFCs2_TDEP, $\kappa_L^{\text{p+c}}$ only changes slightly, confirming that phonon frequency renormalization is

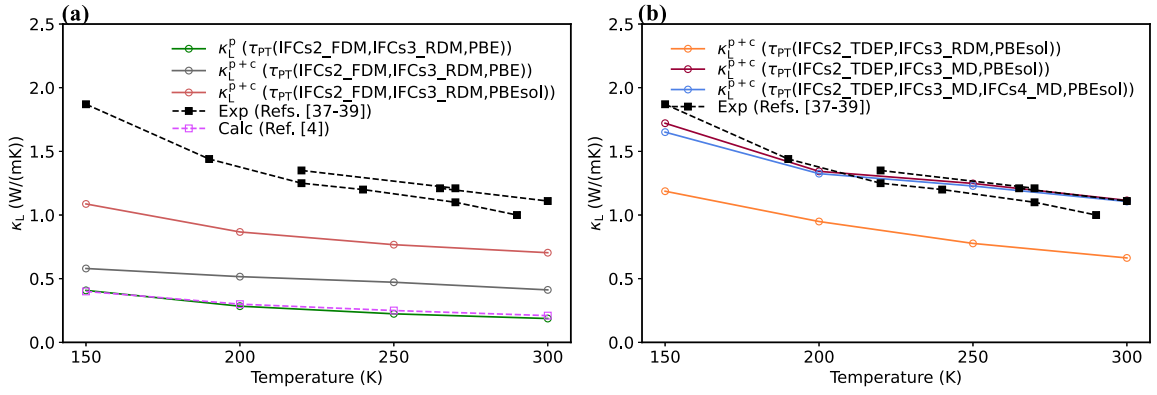


FIG. 1. (a,b) Temperature-dependent κ_L of AgCl calculated using different sets of IFCs with PBE and PBEsol functionals under the UT [6]. IFCs2, IFCs3, and IFCs4 stand for the second-, third-, and fourth-order IFCs, respectively. Configurations used for fitting the IFCs are generated by performing MD simulations [32] based on our NEP, and via the RDM from a normal distribution with a standard deviation of 0.025 Å. IFCs2_FDM and IFCs2_TDEP are extracted using the FDM and TDEP methods, respectively. The black solid symbols represent the experimental results taken from Refs. [37–39]. The purple square symbols stand for the theoretical data reported in Ref. [4].

insignificant to computing the κ_L of AgCl, as displayed in Figs. 1(a) and 1(b).

A recent study demonstrated that largely displaced configurations are necessary to accurately extract the third-order IFCs for group-III phosphides [42]. Thus, we further investigate a different method for calculating the third-order IFCs and the effect on the κ_L of AgCl. The calculated κ_L^p increases significantly when we use IFCs3_MD, as shown in Figs. S4(c) and S4(d), illustrating that an accurate calculation of the third-order IFCs is of great significance for predicting the κ_L of AgCl. Once the coherence contribution is also considered, a good agreement is obtained with the experimental results [37–39], as shown in Fig. 1(b). The third-order IFCs calculated based on MD configurations can decrease the phonon linewidths, as shown in Fig. S5(b), and thus increase the κ_L^p . The atomic displacements of Ag and Cl atoms increase significantly with elevating temperature, as described by the comparably large mean square displacements in Fig. S9. Therefore, extracting the third-order IFCs of AgCl from con-

figurations generated by MD simulations is more reasonable. We further extend our calculations to silver halides AgBr and AgI, and the results are shown in Fig. 2. We find that the κ_L^{p+c} of AgBr computed using IFCs2_TDEP and IFCs3_MD with PBEsol functional agrees well with the experimental results [43–45], while for AgI, the calculated κ_L^{p+c} apparently overestimates the experiments [8]. When the four-phonon scatterings are also considered, the κ_L^{p+c} significantly decreases from 4.88 to 1.21 W m⁻¹K⁻¹ at 300 K, but it still overestimates the experimental value (0.42 W m⁻¹K⁻¹), as shown in Fig. 2(b). We further compute the phonon linewidths from PT using the IFCs fitted to MD configurations at 300 K, as shown in Fig. 3(b). It is seen that the four-phonon linewidths are non-negligible, especially for the low-frequency modes, which usually contribute most to the thermal transport. In addition, we have calculated the temperature-dependent κ_L of AgI from HNEMD simulations with our NEP, and a good agreement with the experiment [8] is observed, as shown in Fig. 2(b).

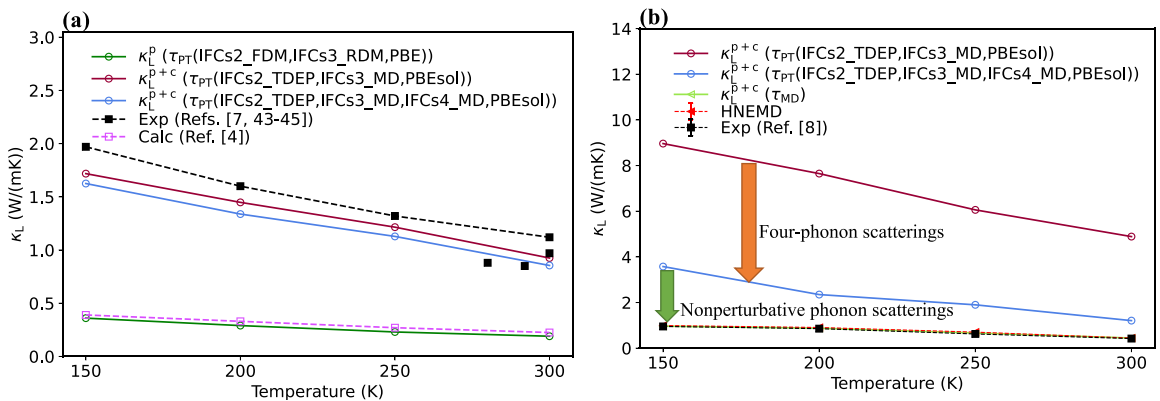


FIG. 2. (a) Temperature-dependent κ_L^{p+c} of AgBr calculated using different sets of IFCs under the UT [6]. The black solid symbols represent the experimental results from Refs. [7,43–45]. The mallow purple hollow symbols stand for the theoretical data reported in Ref. [4]. (b) κ_L^{p+c} of AgI computed using the different sets of IFCs. κ_L calculated using the phonon lifetimes (τ_{MD}) extracted from MD simulations and that from HNEMD simulations [35,46] based on NEP are also shown for comparisons. The black solid symbols represent the experimental results from Ref. [8].

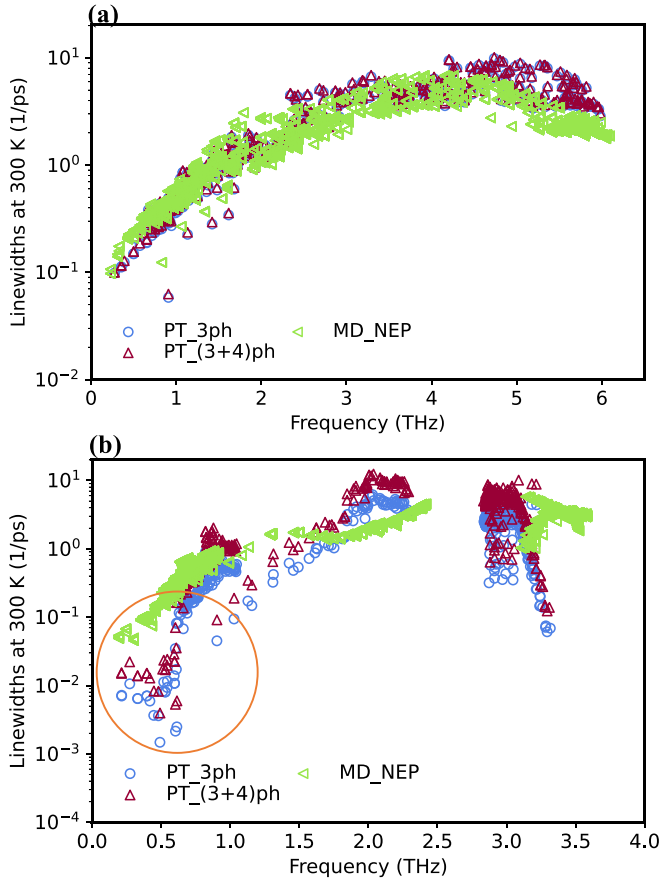


FIG. 3. Phonon linewidths of AgCl (a) and AgI (b) calculated from PT and MD simulations at 300 K. PT_{3ph} and PT_{(3+4)ph} represent the phonon linewidths computed using only the third-order and both of the third- and fourth-order IFCs, respectively. MD_{NEP} denotes the phonon linewidths calculated from MD simulations using our NEP.

The overestimated κ_L^{p+c} of AgI obtained from UT may be related to the inaccurate phonon linewidths; thus, we compare the phonon linewidths obtained from PT with that obtained from MD simulations using the normal-mode-decomposition technique [22], as displayed in Fig. 3(b). We find that the MD phonon linewidths, which include full-order lattice anharmonicity, are significantly larger than those obtained from PT, suggesting that the higher-than-fourth-order lattice anharmonicity can be crucial for calculating the phonon linewidths and thus the κ_L of AgI. Therefore, we further compute the κ_L^{p+c} using the MD phonon lifetimes τ_{MD} , and it shows a better agreement with the experimental values [8] and the HNEMD simulations over a temperature range from 150 to 300 K, as shown in Fig. 2(b). We also find that the population term ($0.21 \text{ W m}^{-1} \text{ K}^{-1}$) of AgI is comparable with the coherence's contribution ($0.23 \text{ W m}^{-1} \text{ K}^{-1}$) at 300 K, as displayed in Fig. S8, indicating that the coherence channel is of great importance to describing the thermal transport. On the other hand, we find that the difference of the phonon linewidths of AgCl between PT_{3ph}, PT_{(3+4)ph}, and MD_{NEP} is much smaller, as shown in Fig. 3(a), suggesting that the higher-than-third-order lattice anharmonicity is insignificant to the lattice thermal transport.

To further reveal the different thermal transport mechanisms between AgCl and AgI, we calculate the three- and four-phonon WPS, as shown in Figs. 4(a) and 4(b). From the phonon dispersions of AgI given in Fig. S3(b), we can observe that the transverse acoustic (TA) branches ($\sim 0.7 \text{ THz}$) are almost nondispersive near the high symmetry X point, and the energy of the longitudinal acoustic (LA) branch is higher than double of the energy of the TA branches. Moreover, as illustrated in Fig. S11(b), the combination of one TA phonon (TA1 or TA2) and one LA phonon can easily create one new LA phonon and one TA phonon (TA1 or TA2) through the four-phonon recombination process due to the simple satisfaction of energy and momentum conservations. In comparison, the absorption of three-phonon scattering is limited by the energy conservation, as depicted in Fig. S11(a). Therefore, due to the conservations of phonon energy and momentum, three-phonon channels involving the low-frequency phonons are restricted, as indicated by the highlighted dip in Fig. 4(a) for AgI. In contrast, no restriction on the three-phonon phase space is observed for AgCl. In addition, for the four-phonon WPS shown in Fig. 4(b), we see that the redistribution channel is also restricted for the low-frequency phonons (below 0.5 THz) in AgI. Thus, the simultaneous restrictions of the three- and four-phonon WPS at low-frequency regions can lead to a more important role of the higher-order lattice anharmonicity in the thermal transport of AgI.

Although the significant role of the higher-than-fourth-order lattice anharmonicity in the specific optical phonon modes at the zone center has been demonstrated in zincblende III-V compounds [16] such as InP and BN, a study over the entire Brillouin zone is challenging due to the complex PT framework. Herein, we take AgI as an example and further calculate the phonon linewidths using the normal-mode-decomposition technique [22] and MD simulations based on a Taylor expansion force constant potential (FCP) [47] at 100 K, as shown in Fig. S6(b). Results are obtained only at low temperatures because the MD simulations based on the FCP of AgI become unstable over 100 K. We observe that the phonon linewidths computed using NEP and the sixth-order FCP at 100 K are comparable, especially those of the low-frequency phonons, indicating that the seventh- or higher-order lattice anharmonicity plays a minor role in the phonon scattering of AgI at low temperatures. However, the phonon linewidths calculated based on the fourth-order FCP are much smaller than those from the sixth-order FCP in the low-frequency ($\sim 0.2\text{--}0.8 \text{ THz}$) region, suggesting the importance of the fifth- and sixth-order lattice anharmonicity in the accurate calculation of the phonon linewidths and the κ_L of AgI. In other words, it is necessary to consider the higher-than-fourth-order lattice anharmonicity when calculating the κ_L of AgI even at low temperatures.

IV. CONCLUSION

In summary, using accurate machine learning NEP, we systematically study the phonon thermal transport of AgX under the framework of UT and MD simulations. Our results show that an accurate calculation of the third-order IFCs is important to predict the κ_L of AgX, and we also demonstrate that coherence contribution is considerable in

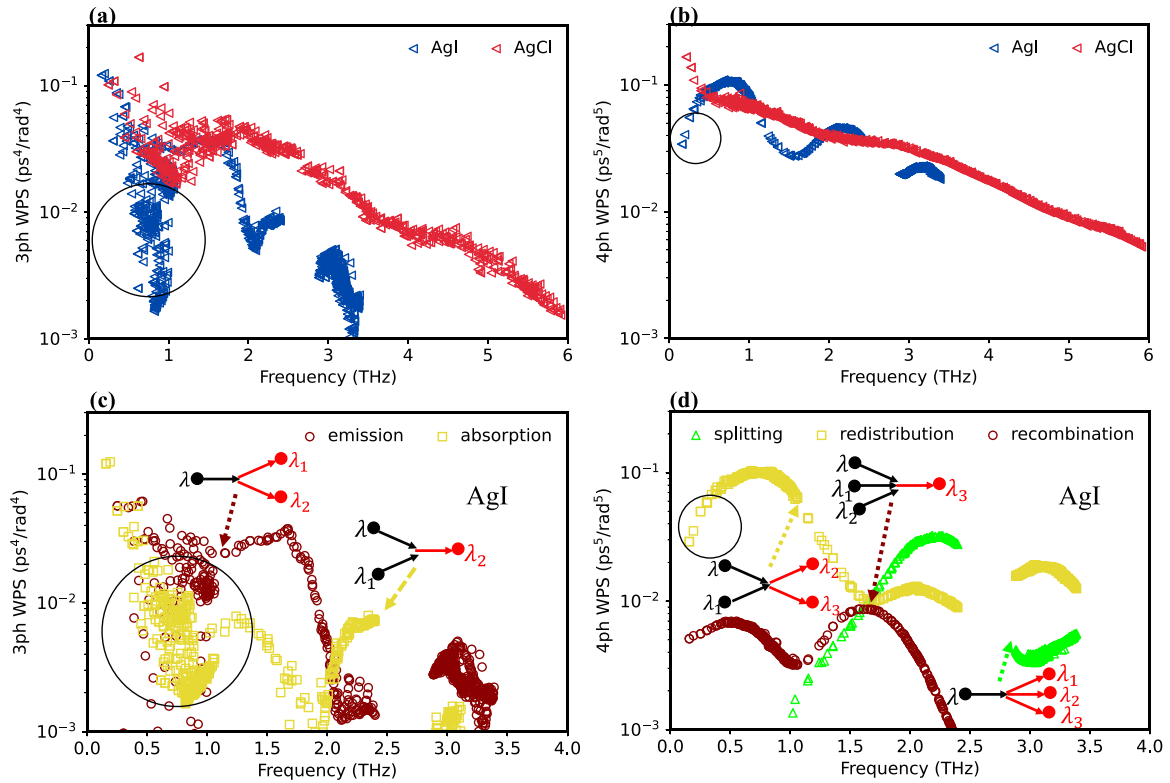


FIG. 4. Three- (a) and four-phonon (b) WPS of AgCl and AgI at 300 K. Mode-resolved three- (c) and four-phonon (d) WPS of AgI calculated at 300 K. Restricted phase space is observed inside the circled areas.

these materials. Our MD simulations with NEP explicitly demonstrate the important contribution of the higher-than-fourth-order phonon scattering to the phonon linewidths and the κ_L of AgI. Our theoretical analysis suggests that this can be attributed to the simultaneous restrictions of P_3 and P_4 . Thus, the κ_L calculated using the MD phonon linewidths agree better with the experiments and the HNEMD simulations of AgI.

ACKNOWLEDGMENTS

This work is supported by the Research Grants Council of Hong Kong (Grants No. 17318122 and No. 17306721). The authors are grateful for the research computing facilities offered by ITS, HKU. Z.Z. acknowledges the European Union's Horizon 2020 research and innovation program under the Marie Skłodowska-Curie Grant Agreement No. 101034413.

- [1] N. Kakuta, N. Goto, H. Ohkita, and T. Mizushima, Silver bromide as a photocatalyst for hydrogen generation from $\text{CH}_3\text{OH}/\text{H}_2$ solution, *J. Phys. Chem. B* **103**, 5917 (1999).
- [2] X. Yang, Z. Xiong, Y. Chen, Y. Ren, L. Zhou, H. Li, Y. Zhou, F. Pan, and S.-T. Han, A self-powered artificial retina perception system for image preprocessing based on photovoltaic devices and memristive arrays, *Nano Energy* **78**, 105246 (2020).
- [3] T. Takahashi, E. Nomura, and O. Yamamoto, Solid state ionic. High ionic conductivity solid in silver halide-silver sulphate system, *J. Appl. Electrochem.* **2**, 51 (1972).
- [4] X. Yang, Z. Dai, Y. Zhao, and S. Meng, Superhigh thermoelectric figure of merit in silver halides AgCl and AgBr from first principles, [arXiv:1904.06010](https://arxiv.org/abs/1904.06010).
- [5] Y. Xia, V. I. Hegde, K. Pal, X. Hua, D. Gaines, S. Patel, J. He, M. Aykol, and C. Wolverton, High-throughput study of lattice thermal conductivity in binary rocksalt and zinc blende compounds including higher-order anharmonicity, *Phys. Rev. X* **10**, 041029 (2020).
- [6] M. Simoncelli, N. Marzari, and F. Mauri, Unified theory of thermal transport in crystals and glasses, *Nat. Phys.* **15**, 809 (2019).
- [7] R. Ross, P. Andersson, and G. Bäckström, Thermal conductivity and heat capacity of solid AgCl under pressure, *Int. J. Thermophys.* **2**, 289 (1981).
- [8] M. Goetz and J. Cowen, The thermal conductivity of silver iodide, *Solid State Commun.* **41**, 293 (1982).
- [9] Y. Wang, Q. Gan, M. Hu, J. Li, L. Xie, and J. He, Anharmonic lattice dynamics and the origin of intrinsic ultralow thermal conductivity in AgI materials, *Phys. Rev. B* **107**, 064308 (2023).
- [10] Z. Zeng, C. Zhang, H. Yu, W. Li, Y. Pei, and Y. Chen, Ultralow and glass-like lattice thermal conductivity in crystalline BaAg_2Te_2 : Strong fourth-order anharmonicity and crucial diffusive thermal transport, *Mater. Today Phys.* **21**, 100487 (2021).
- [11] Y. Xia, K. Pal, J. He, V. Ozoliņš, and C. Wolverton, Particlelike phonon propagation dominates ultralow lattice thermal

- conductivity in crystalline Ti_3VSe_4 , *Phys. Rev. Lett.* **124**, 065901 (2020).
- [12] N. Ouyang, C. Wang, and Y. Chen, Role of alloying in the phonon and thermal transport of SnS-SnSe across the phase transition, *Mater. Today Phys.* **28**, 100890 (2022).
- [13] T. Feng, L. Lindsay, and X. Ruan, Four-phonon scattering significantly reduces intrinsic thermal conductivity of solids, *Phys. Rev. B* **96**, 161201(R) (2017).
- [14] A. Kundu, X. Yang, J. Ma, T. Feng, J. Carrete, X. Ruan, G. K. H. Madsen, and W. Li, Ultrahigh thermal conductivity of θ -phase tantalum nitride, *Phys. Rev. Lett.* **126**, 115901 (2021).
- [15] Z. Zeng, C. Zhang, Y. Xia, Z. Fan, C. Wolverton, and Y. Chen, Nonperturbative phonon scatterings and the two-channel thermal transport in Ti_3VSe_4 , *Phys. Rev. B* **103**, 224307 (2021).
- [16] X. Yang, T. Feng, J. Li, and X. Ruan, Evidence of fifth- and higher-order phonon scattering entropy of zone-center optical phonons, *Phys. Rev. B* **105**, 115205 (2022).
- [17] Q. Wang, Z. Zeng, and Y. Chen, Revisiting phonon transport in perovskite SrTiO_3 : Anharmonic phonon renormalization and four-phonon scattering, *Phys. Rev. B* **104**, 235205 (2021).
- [18] Z. Zeng, C. Chen, C. Zhang, Q. Zhang, and Y. Chen, Critical phonon frequency renormalization and dual phonon coexistence in layered Ruddlesden-Popper inorganic perovskites, *Phys. Rev. B* **105**, 184303 (2022).
- [19] T. Tadano and S. Tsuneyuki, Quartic anharmonicity of rattlers and its effect on lattice thermal conductivity of clathrates from first principles, *Phys. Rev. Lett.* **120**, 105901 (2018).
- [20] Z. Fan, Z. Zeng, C. Zhang, Y. Wang, K. Song, H. Dong, Y. Chen, and T. Ala-Nissila, Neuroevolution machine learning potentials: Combining high accuracy and low cost in atomistic simulations and application to heat transport, *Phys. Rev. B* **104**, 104309 (2021).
- [21] L. Isaeva, G. Barbalinardo, D. Donadio, and S. Baroni, Modeling heat transport in crystals and glasses from a unified lattice-dynamical approach, *Nat. Commun.* **10**, 3853 (2019).
- [22] A. Carreras, A. Togo, and I. Tanaka, DynaPhoPy: A code for extracting phonon quasiparticles from molecular dynamics simulations, *Comput. Phys. Commun.* **221**, 221 (2017).
- [23] T. Hansson, C. Oostenbrink, and W. van Gunsteren, Molecular dynamics simulations, *Curr. Opin. Struct. Biol.* **12**, 190 (2002).
- [24] G. Kresse and J. Furthmüller, Efficient iterative schemes for *ab initio* total-energy calculations using a plane-wave basis set, *Phys. Rev. B* **54**, 11169 (1996).
- [25] P. E. Blöchl, Projector augmented-wave method, *Phys. Rev. B* **50**, 17953 (1994).
- [26] J. P. Perdew, A. Ruzsinszky, G. I. Csonka, O. A. Vydrov, G. E. Scuseria, L. A. Constantin, X. Zhou, and K. Burke, Restoring the density-gradient expansion for exchange in solids and surfaces, *Phys. Rev. Lett.* **100**, 136406 (2008).
- [27] See Supplemental Material at <http://link.aps.org/supplemental/10.1103/PhysRevB.108.174302> for more computational details. This includes Refs. [32,48–50].
- [28] B. Lawn, Thermal expansion of silver halides, *Acta Crystallogr.* **16**, 1163 (1963).
- [29] F. Eriksson, E. Fransson, and P. Erhart, The hiPhive package for the extraction of high-order force constants by machine learning, *Adv. Theory Simul.* **2**, 1800184 (2019).
- [30] O. Hellman, P. Steneteg, I. A. Abrikosov, and S. I. Simak, Temperature dependent effective potential method for accurate free energy calculations of solids, *Phys. Rev. B* **87**, 104111 (2013).
- [31] O. Hellman, I. A. Abrikosov, and S. Simak, Lattice dynamics of anharmonic solids from first principles, *Phys. Rev. B* **84**, 180301(R) (2011).
- [32] Z. Fan, Y. Wang, P. Ying, K. Song, J. Wang, Y. Wang, Z. Zeng, K. Xu, E. Lindgren, J. M. Rahm *et al.*, GPUMD: A package for constructing accurate machine-learned potentials and performing highly efficient atomistic simulations, *J. Chem. Phys.* **157**, 114801 (2022).
- [33] Y. Xia, V. Ozoliņš, and C. Wolverton, Microscopic mechanisms of glasslike lattice thermal transport in cubic $\text{Cu}_{12}\text{Sb}_4\text{S}_{13}$ tetrahedrites, *Phys. Rev. Lett.* **125**, 085901 (2020).
- [34] W. Li and N. Mingo, Ultralow lattice thermal conductivity of the fully filled skutterudite $\text{YbFe}_4\text{Sb}_{12}$ due to the flat avoided-crossing filler modes, *Phys. Rev. B* **91**, 144304 (2015).
- [35] Z. Fan, H. Dong, A. Harju, and T. Ala-Nissila, Homogeneous nonequilibrium molecular dynamics method for heat transport and spectral decomposition with many-body potentials, *Phys. Rev. B* **99**, 064308 (2019).
- [36] D. J. Evans, Homogeneous NEMD algorithm for thermal conductivity: application of non-canonical linear response theory, *Phys. Lett. A* **91**, 457 (1982).
- [37] A. Maqsood, M. Anis-ur Rehman, K. Kamran, and I. H. Gul, Thermophysical properties of AgCl in the temperature range 77–300 K, *J. Phys. D* **37**, 1845 (2004).
- [38] D. R. Lide, *CRC Handbook of Chemistry and Physics* Vol. 85 (CRC, Boca Raton, 2004).
- [39] K. A. McCarthy and S. S. Ballard, New data on the thermal conductivity of optical crystals, *J. Opt. Soc. Am.* **41**, 1062 (1951).
- [40] L. Chaput, A. Togo, I. Tanaka, and G. Hug, Phonon-phonon interactions in transition metals, *Phys. Rev. B* **84**, 094302 (2011).
- [41] K. Fischer, Lattice dynamics and anharmonic effects in AgCl , *Phys. Status Solidi B* **66**, 295 (1974).
- [42] B. Dongre, J. Carrete, N. Mingo, and G. K. H. Madsen, Thermal conductivity of group-III phosphides: The special case of GaP , *Phys. Rev. B* **106**, 205202 (2022).
- [43] K. Kamran, M. Anis-ur Rehman, and A. Maqsood, Thermal and electrical properties of crystalline silver bromide, *J. Phys. D* **40**, 869 (2007).
- [44] T. Pochapsky, Heat capacity and thermal diffusivity of silver bromide, *J. Chem. Phys.* **21**, 1539 (1953).
- [45] E. Washburn, *International Critical Tables*, 1st ed. Vol. 1 (McGraw-Hill, New York, 1926).
- [46] B. Dongre, T. Wang, and G. K. Madsen, Comparison of the Green-Kubo and homogeneous non-equilibrium molecular dynamics methods for calculating thermal conductivity, *Modell. Simul. Mater. Sci. Eng.* **25**, 054001 (2017).
- [47] J. Brorsson, A. Hashemi, Z. Fan, E. Fransson, F. Eriksson, T. Ala-Nissila, A. V. Krashennnikov, H.-P. Komsa, and P. Erhart, Efficient calculation of the lattice thermal conductivity by atomistic simulations with *ab initio* accuracy, *Adv. Theory Simul.* **5**, 2100217 (2022).
- [48] Z. Fan, Improving the accuracy of the neuroevolution machine learning potential for multi-component systems, *J. Phys. D: Condens. Matter* **34**, 125902 (2022).

- [49] C. W. Li, J. Ma, H. B. Cao, A. F. May, D. L. Abernathy, G. Ehlers, C. Hoffmann, X. Wang, T. Hong, A. Huq *et al.* Anharmonicity and atomic distribution of SnTe and PbTe thermoelectrics, [Phys. Rev. B **90**, 214303 \(2014\)](#).
- [50] Y. Lu, T. Sun, and D.-B. Zhang, Lattice anharmonicity, phonon dispersion, and thermal conductivity of PbTe studied by the phonon quasiparticle approach, [Phys. Rev. B **97**, 174304 \(2018\)](#).